Chapter 3: Thermal analysis

3.1 Introduction

A Perkin-Elmer DSC7 with Perkin-Elmer Pyris software was used for thermal analysis of the samples. A small mass (~5 mg) of sample was sealed inside an aluminium can and the difference between heat flow into this can and an empty reference can was measured as a function of temperature. The input power is controlled by a feedback loop which attempts to make the sample and reference can temperatures equal. In practice, small temperature differences do exist, their magnitude determined by the temperature ramp, sample mass and phase change kinetics. In this study, isothermal temperatures were employed for a time-domain analyses of crystallisation processes, followed by constant rate temperature ramps for melting behaviour analysis.

Indium and sapphire were used to calibrate the DSC. Sapphire has a known heat capacity of 112 J $°C^{-1}$ mol^{-1} at 600 °K [3.1], and was therefore used to calibrate the instrument for heat flow. High purity indium has a known melting temperature of 156.6 °C and was used for temperature axis calibration. Indium was also used for balance calibration, to minimise asymmetry between the furnaces. Cans containing ~50 µg and ~200 µg of indium were placed in the reference and sample furnaces respectively. They were heated at 1 °C min^{-1} between 150 °C and 160 °C. A single peak was observed if the instrument was sufficiently balanced. Conversely, peak separation was observed if there was an imbalance greater than 0.1 °C.

For accurate temperature calibration, the effect of ramp rate had to be taken into account. This is because the temperature differential, ideally zero, takes a finite value which increases with ramp rate and sample mass. For accurate temperature calibration it was necessary to record the melting point at 1 °C min^{-1}, 2 °C min^{-1} 5 °C min^{-1} and 10 °C min^{-1} before extrapolating to zero ramp rate for isothermal crystallisation. A strict protocol was adhered to whereby the experiment order was randomised with respect to sample identity and crystallisation temperature, thereby eliminating the effects of instrumental drift from the data.

3.2 Avrami analysis

If a DSC isothermal crystallisation curve is integrated as a function of time, it is possible to analyse the kinetics of crystallisation using Avrami analysis [3.2],[3.3],[3.4]. If one considers nucleation as random events at different locations, the problem can be compared to raindrops of water landing on the surface of water and producing circular wavefronts. Gedde [3.5] gives derivations for the case where all the crystals are nucleated at t=0 (athermal nucleation) and where nucleation occurs (thermal nucleation) at a constant rate. The same general formula applies, however, which after taking into account incomplete crystallisation and volume changes during crystallisation has the form:

$$1-\frac{v_c}{v_\infty}=\exp\left(-K\left[1-v_c\left(\frac{\rho_c-\rho_l}{\rho_l}\right)\right]t^n\right) \qquad (3.1)$$

where v_c and v_∞ are the instantaneous and final crystallinity volume fractions, ρ_c and ρ_l are the densities of the crystal phase and the melt respectively, and n is the Avrami exponent, which depends on the dimensionality of the crystallisation, the mathematical form of the linear crystal growth rate and to what degree the nucleation is thermal or athermal.

Morgan [3.6] gives a thorough discussion of Avrami parameters in the light of first principles derivation, albeit for highly simplified situations. The basic idea is to consider any point in space, P, taking at first the case of athermal nucleation (all nucleation at t=0.) If we imagine a spherical shell defined by $r+dr$ from P, then the probability of an entity originating from that shell and arriving at P before a time t can be calculated. Or, if nucleation is random in space and time (thermal nucleation), any point in the shell might be able to send out an object that might cross P before t during a time equal to $t - r/v$, where v is the linear growth rate. The shell is then integrated between r=0 and r=vt, to produce the degree of unconversion as a function of time. Table 3.1 shows some resulting theoretical Avrami parameters.

Mechanism	N	K
Fibrillar (athermal)	1	$-\frac{\pi}{2}d^2vw$
Fibrillar (thermal)	2	$-\frac{\pi}{4}d^2v\Omega$
Laminar spherulitic (athermal)	2	$-hv^2w$
Laminar spherulitic (thermal)	3	$-hv^2\frac{\Omega}{2}$
Spherical spherulitic (athermal)	3	$-\frac{4\pi}{3}wv^3$
Spherical spherulitic (thermal)	4	$-\frac{\pi}{3}\Omega v^3$

Table 3.1: Avrami parameters derived by Morgan [3.6]. Key: *d* = diameter of fibre, *v* = linear growth rate, *w* = nucleation density, *Ω* = nucleation rate, *h* = lamellar thickness.

In reality, the values of *n* obtained by experiment are seldom this elegant. The fundamental problem of how to compare growth parameters for different values of *n* has been addressed by Kowaleski and Galeski [3.7]. On the basis that non-integer values of *n* can be attributed to mixed nucleation modes and secondary crystallisation, they argued that an effective 3-dimensional crystallisation rate parameter K_3 can be obtained:

$$K_3 = \frac{4}{3}NG^3 \approx K_{\exp}^{\left(\frac{3}{n}\right)} \qquad (3.2)$$

where *N* is the nucleation density and *G* the linear growth rate. K_3 has a consistent dimensionality for comparison across datasets with variable *n*.

However, equation 3.2 makes the assumption that the value of *n* obtained from data analysis is correct. This is unlikely to be the case at low and high isothermal temperatures due to instrumental lag and baseline drift respectively. Figure 3.1 illustrates the integration of a typical power-time curve in order to extract K_3 and *n* from equation 3.1. As the shape of the

instrumental lag depends on the sample mass, it is not appropriate to use the response of an empty can as a baseline. Instead, a common tangent is drawn to the curve either side of the crystallisation event. The signal may be distorted in two ways. The power-time curve may have an approximately correct shape but report a crystallisation onset time which is later than the real crystallisation onset. A non-linear fitting algorithm can then be used to estimate K_{exp} and recover the associated t_0 with n as an independent parameter. This is referred to below as the variable onset method. Only the first 60% of the area was analysed because of the possibility of significant deviation from simple Avrami behaviour at higher degrees of conversion, due to secondary crystallisation processes. Alternatively, crystallisation may be believed to truly begin at the maximum on the left of Figure 3.1, but the shape may nonetheless be distorted by the imposed tangent and baseline drift. In this case, the variable shape method, K_{exp} can be eliminated from equation 3.1 using a two point calibration at t_0 and the time associated with 60% conversion. K_3 can then be transformed from K_{exp} for each trial value of n.

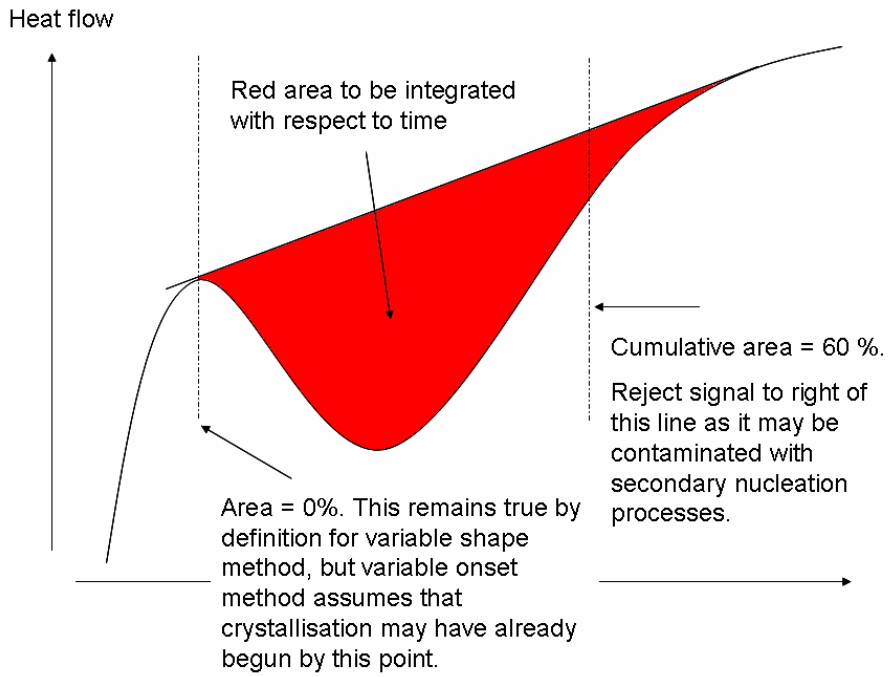

Figure 3.1 Integration of the power flow curve associated with isothermal crystallisation, to aid discussion of variable onset and shape methods in text.

Figure 3.2 compares the values of K_3 obtained for NB0=NC0 and NC10 at a crystallisation temperature of 120 °C. Both variable onset and shape techniques are shown with *n* as an independent variable. The plots answer the question: "if the true, underlying growth dimensionality is *n*, how do the variable onset and variable shape approaches compare?"

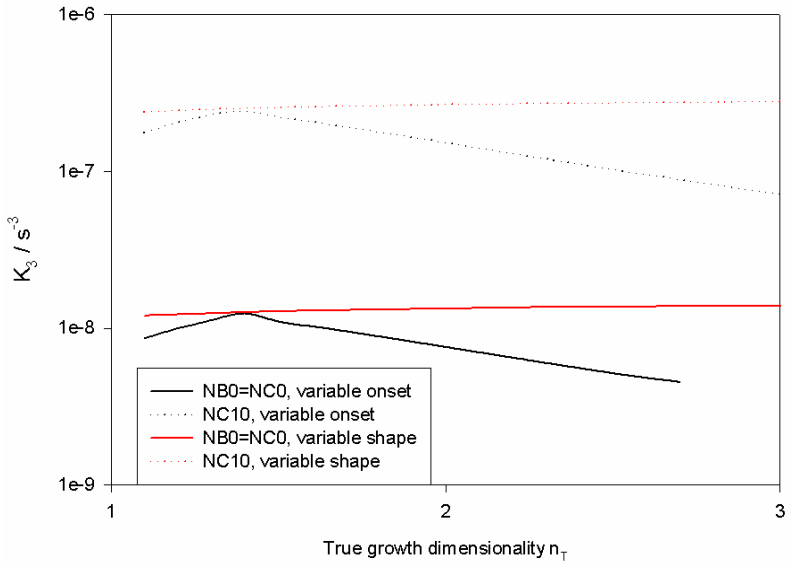

Figure 3.2: Comparison of K_3 obtained for NB0=NC0 and NC10 using variable onset and variable shape methods for a crystallisation temperature of 120 °C. Both techniques lead to the conclusion that K_3 is significantly higher in NC10 than NB0=NC0.

For spherulitic growth, it should be expected that $2<n<3$. At early stages of growth, initially-nucleated lamellae will grow in two dimensions; *n* will then increase as secondary nucleation begins to dominate. For example, Ultra-SAXS has been used to determine a dimensionality of 2.7 for poly((R)-3-hydroxybutyrate) spherulites [3.8]. It is clear in Figure 3.2 that the variable onset and shape curves yield similar values of K_3 at $n \approx 1.4$; this is the point where the best fit for the nonlinear fitting algorithm was obtained. The amount of enthalpy lost at low conversions according to the variable onset method never amounted to more than 5% at high values of *n*, establishing the validity of both techniques for complementary analyses of these data.

Figures 3.3 and 3.4 show that the effective 3-dimensional crystallisation rate is considerably higher in NC10 compared to NB0=NC0 over the temperature range 110 °C – 120 °C. This can be explained in terms of NC10 having either a higher nucleation density or linear growth rate than NB0=NC0. A minimum confidence bound for the increase in K_3 can be obtained by the difference between the variable shape line for NB0=NC0 and the variable onset line for NC10. This value becomes larger if NC10 also has a reduced growth dimensionality.

Analysis becomes more complicated when comparing thermally and athermally nucleating systems. From Table 3.1, we see that for a given growth rate, the estimated value of *N* will be half and one third of the final nucleation densities for thermally nucleating laminar and spherical systems respectively. Together with the fact that at lower temperatures, the plots for NB0=NC0 and NC10 become closer together, it is important to annex a caveat to any inferences about *G* and *N.* The differences in K_3 between NC10 and NB0=NC0 can, in this temperature range, be attributed to increased *G* or *N* provided that either there is no change in the ratio of thermal : athermal nucleation or there is no change in the manner by which the power-time curve is distorted by the instrumental response. These caveats can be relaxed at the higher temperatures shown in Figures 3.2 and 3.3. As the form of the relationship between the variable onset and variable shape lines is approximately the same for all temperatures, all estimation of K_3 in the experiments below are obtained using the variable onset approach with *n* as a free parameter.

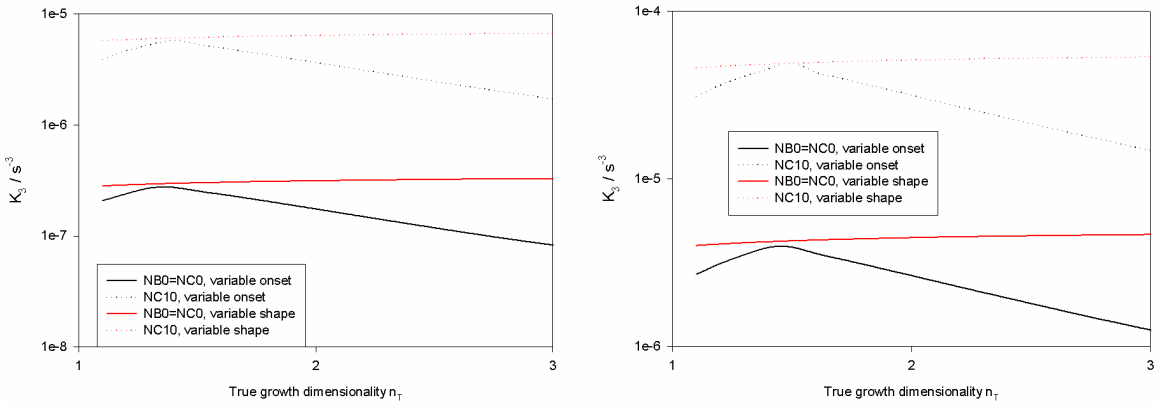

Figure 3.3: As Figure 3.2, but for crystallisation temperatures of 118 °C (left) and 116 °C (right.)

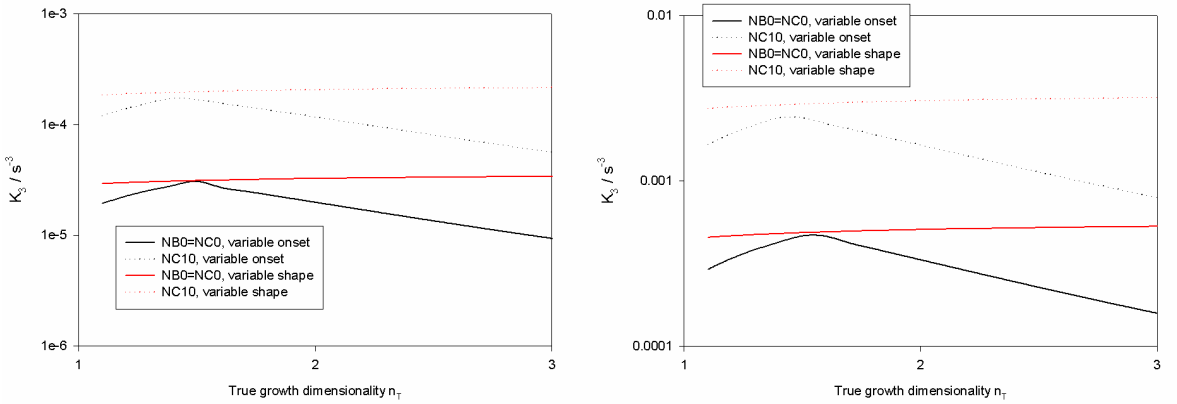

Figure 3.4: As Figure 3.3, but for crystallisation temperatures of 114 °C (left) and 110 °C (right.) At lower temperatures, the conclusion that NC10 has a higher K_3 than NB0=NC0 remains, provided there is no change in the relative validity of the variable onset and variable shape methods.

It was hoped that hotstage experiments would enable direct measurement of *G*. Vaughan [3.9] measured the spherulite diameter growth rates in a material nominally identical to NB0=NC0 at various isothermal crystallisation temperatures. Nucleation densities were then estimated using equation 3.2 and compared to a material nominally identical to NC10. It was assumed that the growth rates in the two materials were equal. (As will be seen in the next chapter, NC10 exhibits very disordered morphologies, and it was not possible for the growth rates in its nominally equivalent counterpart to be measured.) It was found that the predicted nucleation densities for each material were approximately constant between 115 °C and 120 °C, at ~1e+10 and ~1e+11 cm^{-3} for the unfilled and filled materials respectively.

However, the predicted nucleation density of the unfilled material was an order of magnitude higher than that observed in the corresponding SEM images, which are comparable to those obtained for NB0=NC0 in the next chapter. Nucleation densities can be obtained from SEM images simply by counting the number of spherulites sectioned by the image plane and raising the corresponding number density to a power of 1.5 to convert from two to three dimensions. Since it is inconceivable that this method should undercount the number of objects by an order of magnitude, the absolute numbers obtained through comparing Avrami K_3 values with hotstage-derived growth rates should be treated with caution.

In the next chapter, it will be seen that the Nanoblend-based materials exhibit morphologies which are much more similar to NB0=NC0 than the Nanocor-based materials. It was therefore thought that it might be possible to measure their growth rates directly. A Mettler Toledo FP82HT hotstage was mounted on an optical microscope together with a Mettler Toledo FP90 central processor. In order to prepare samples without any shear history which would increase the nucleation density, the materials were dissolved in boiling xylene. Approximately 5 drops of the solution were deposited onto a glass slide with a pipette, leaving films ~ 50 μm thick after solvent evaporation. Initially, crossed polars were used to image the growing spherulites. However, it was found that the glass slide was massively nucleating as a consequence of the maleic anhydride in the filled systems. Attempts were made to use kapton film as an alternative substrate, but it proved too difficult to image the growing spherulites due to depolarisation of the light by the film. We therefore conclude that it is not possible to obtain reliable information on the crystallisation kinetics of the Nanoblend-based systems by optical microscopy unless a substrate is found which passes polarised light but does not interact with maleic anhydride. The discussion in this chapter therefore considers changes in K_3 as a lumped parameter for N and G.

The K_3 parameters for the Nanoblend-based systems as a function of loading level are shown in Figure 3.5. Assuming a constant nucleation density, the conversion rate is only a very weak, non-monotonic function of loading level. The linear material is virtually unaffected by the presence of the nanofiller, though a subtle effect is nonetheless apparent. If the data are ranked in terms of K_3 at each temperature, the values of K_3 for NB0=NC0 and NB10 are always higher than those for NB5 and NB20. Since the a priori probability of this happening by chance is only 20%, we must consider the possibility that subtle effects are at work here. This is more clearly seen in Figure 3.6, in which the effective crystallisation parameters have been normalised relative to the unfilled material.

The loading level dependence of K_3 for the Nanocor-based systems is shown in Figure 3.7, where the behaviour of NC5 falls neatly between NB0=NC0 and NC10. Note that K_3 is not significantly higher in NC20 than

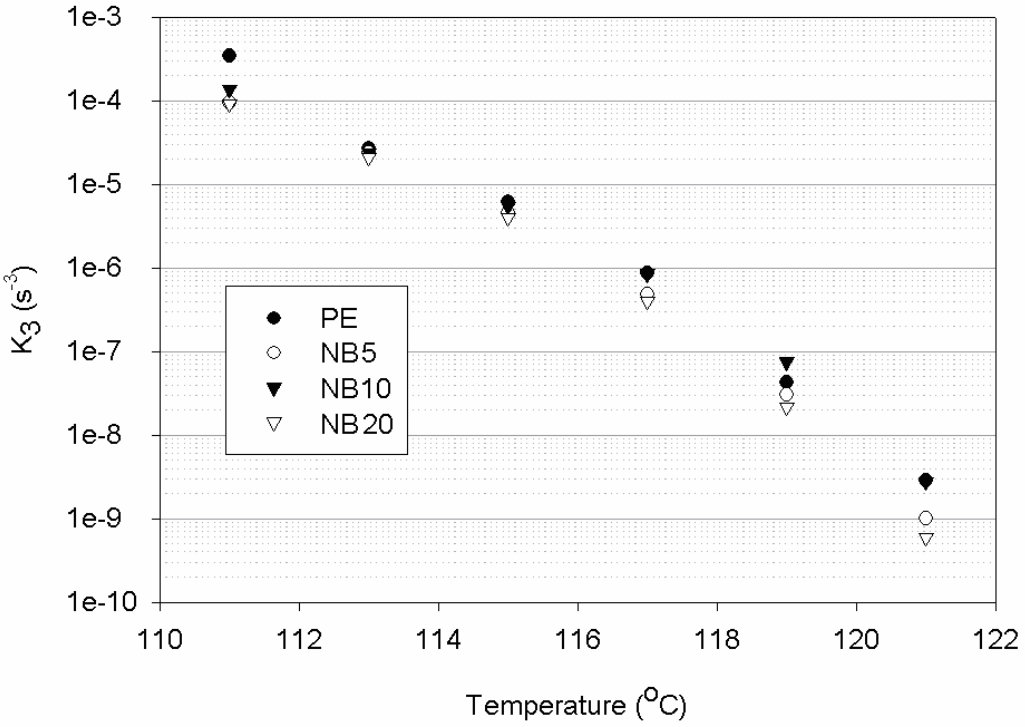

Figure 3.5: K_3 data for Nanoblend-filled systems. Any changes in the overall crystallisation kinetics are subtle.

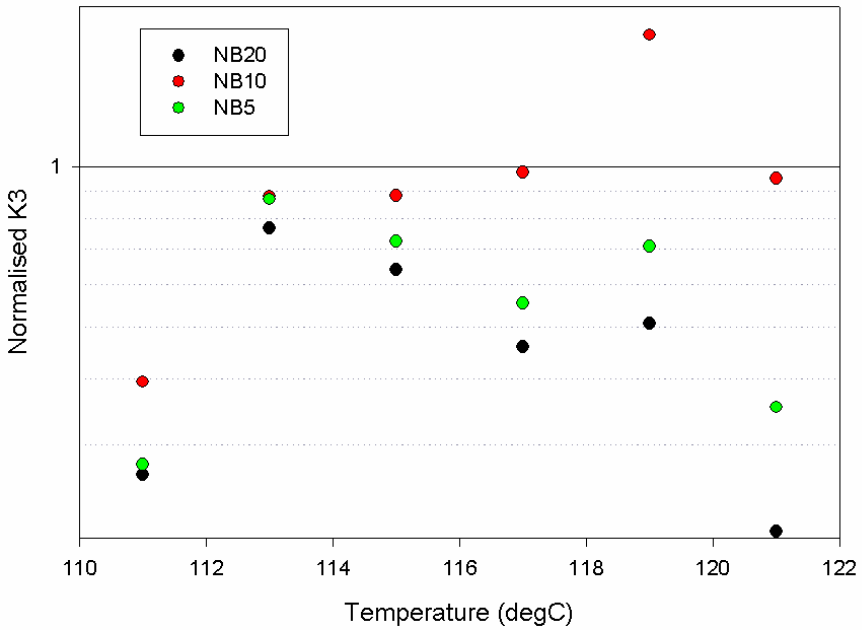

Figure 3.6: K_3 data from Figure 3.5, normalised to NB0=NC0. Subtle processes are affecting the kinetics.

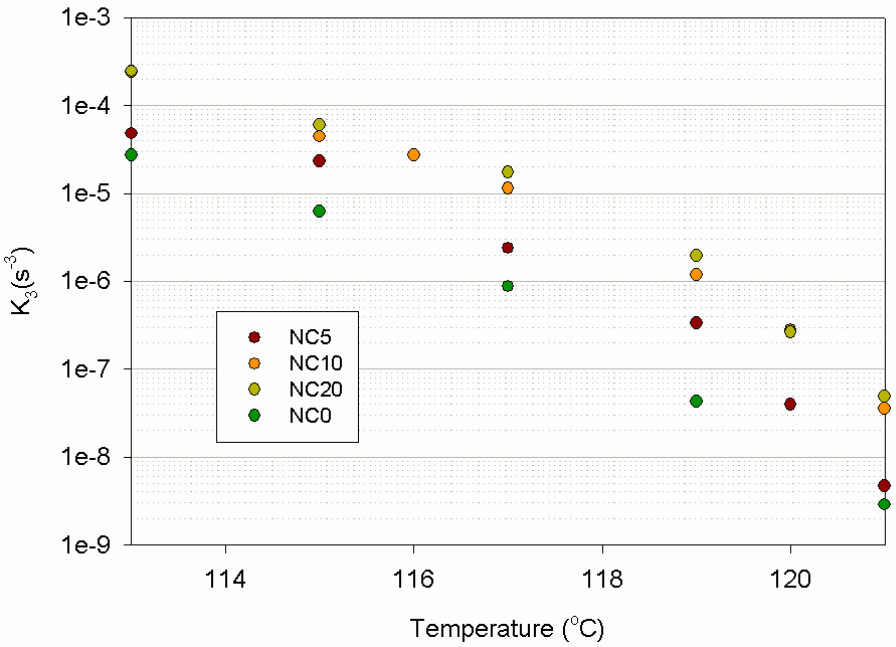

Figure 3.7: Dependence of K_3 on loading level for Nanocor-based systems. Crystallisation rate enhancement has saturated between NC10 and NC20.

NC10, implying that either *N* or *G* saturates between the loading levels associated with these materials.

An attempt was made to enhance the PE-MMT interactions in a Nanoblend-based composite by using a MA-grafted linear material (Polybond 3009, Chemtura Corp.) in place of the non-maleated BP Rigidex 160-25. The structure of MA is shown in Figure 3.8; interactions with the clay should be enhanced through the double-bonded oxygens. Neutron scattering has been used to elucidate the structure of MA-g-PE [3.10]. It was found that the most predominant structures are short chains of oligo-MA with a saturated terminal group, together with less common long chains terminating in an unsaturated group. The materials were extruded in the same way as the non-maleated systems. They are given the nomenclature NB0 (MA) and NB10 (MA) accordingly. Figure 3.9 shows that even if the linear component is maleated, the crystallisation kinetics are not affected by the clay.

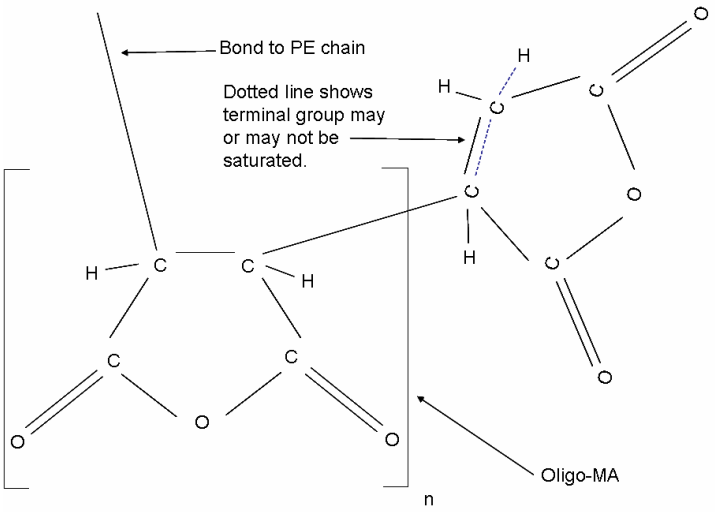

Figure 3.8: Structure of a maleic anhydride graft. Bond lengths not to scale.

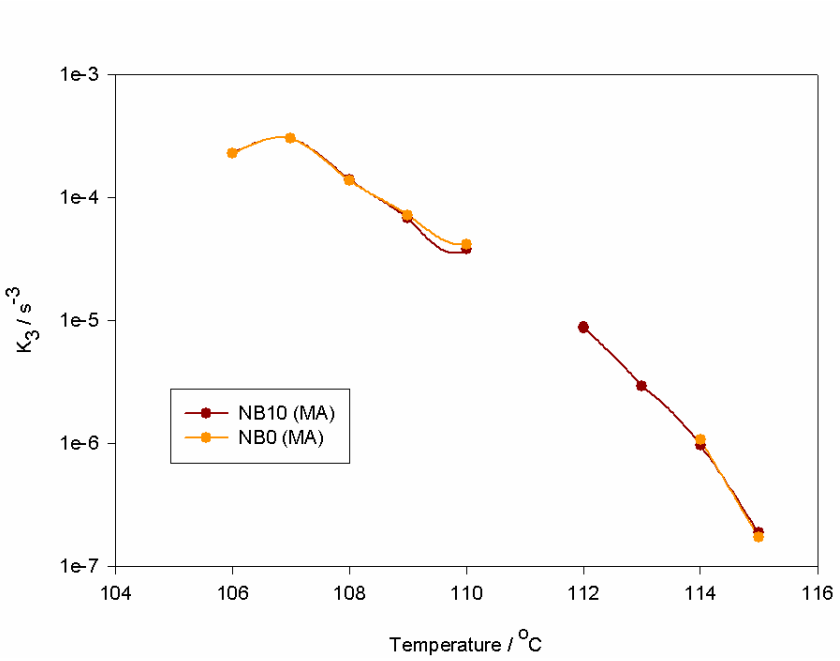

Figure 3.9: K_3 parameters for NB10 (MA) and NB0 (MA). No differences can be seen between the materials.

3.3 Melting behaviour

After each isothermal crystallisation event, the materials were driven to a quench at 50 °C before being heated at 10 °C min^{-1}. It was found that by normalising the data relative to the quench peak and to the value at 140 °C for each trace, baseline drift could be effectively removed from the data. Data corresponding to crystallisation at 113 °C are shown in Figure 3.10. The principal features are as expected for these blend compositions [3.11-3.12]. Branched and defective linear material that is not able to crystallise isothermally will crystallise during quenching, producing the lower melting peak "A." Some of this non-isothermal material will nucleate on the isothermal crystals very early in the quenching process, giving rise to the smaller peak labelled "B." Isothermally crystallised lamellar segments have an initial size distribution which changes during melting as some grow at the expense of others, leading to lamellar thickening. This gives rise to the dominant melting peak several degrees higher than the isothermal crystallisation temperature.

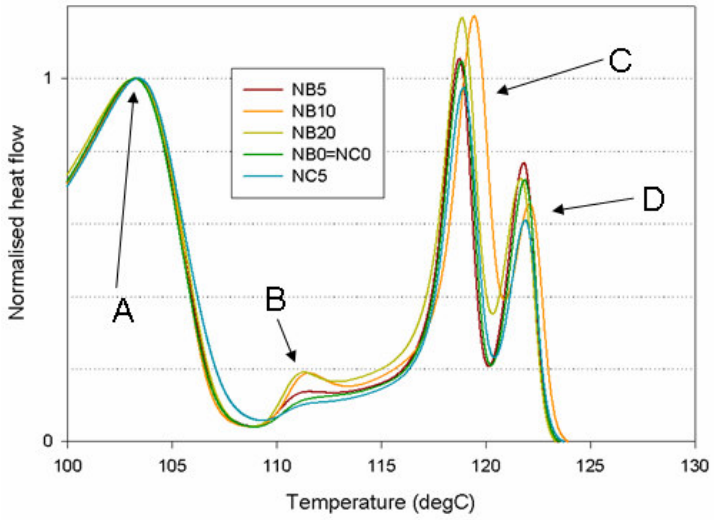

Figure 3.10: Melting endotherms for materials crystallised at 113 °C. Standard features for polyethylene labelled and discussed in text.

At large enough undercoolings and ramp rates, a double peak arises out of this kinetically-limited process, leading to the double crystalline peak labelled "C" and "D." Figure 3.11 is a collection of melting endotherms for all materials and crystallisation temperatures.

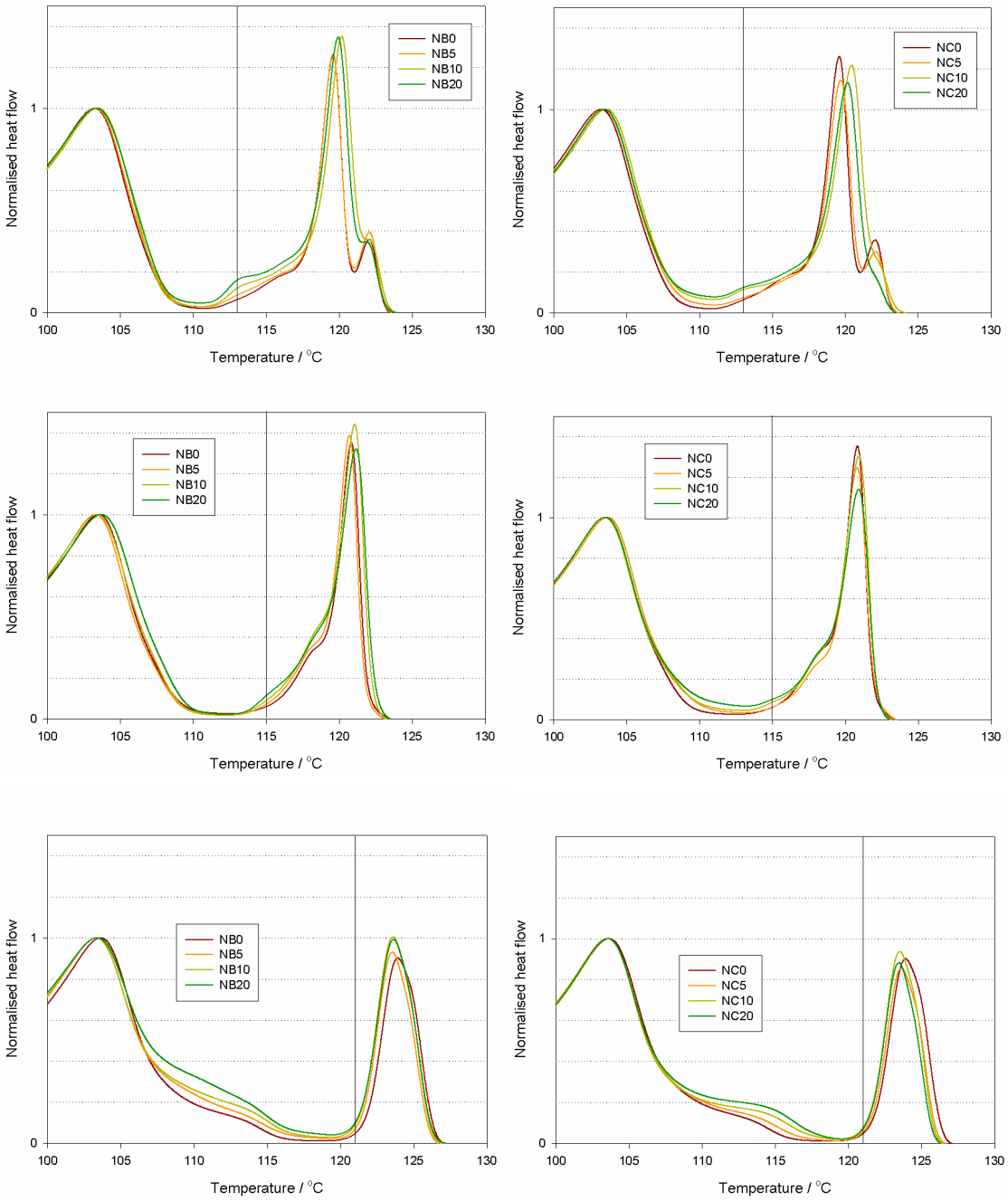

Figure 3.11: Melting endotherms for all materials. Vertical line indicates crystallisation temperature. Lamellar thickening appears to be greater in NB10, NB20, NC10 and NC20 at 113 °C and in NB10 and NB20 at 115 °C.

Two conclusions can be drawn from Figure 3.11:

● Both masterbatch systems show similar behaviour following crystallisation at 113 °C. NB10, NB20, NC10 and NC20 all demonstrate reduced annealing and increased lamellar thickening effects. In NB10 and NB20, pronounced lamellar thickening also occurs following crystallisation at 115 °C, whereas this is not apparent in the Nanocor-based systems.

● At 113 °C and 121 °C, the amount of feature "B" increases with loading level for both masterbatches, although the precise behaviour of this crystal population is subtle. The feature is largely suppressed at 115 °C and 117 °C (not shown.)

3.4 Analysis of crystallisation and melting enthalpies

Raw crystallisation enthalpies for all materials are shown in Figure 3.12. Broadly, the crystallisation enthalpies increase with decreasing temperature. This is due to increasing amounts of cocrystallisation between the predominantly-branched and predominantly-linear fractions and is to be expected from these materials [3.13]. The fact that the 119 °C data are not consistent with this trend can be attributed to baseline drift at longer times. These data alone are not easily interpreted as they do not consider how much of the masterbatch polymers are able to crystallise isothermally.

If we assume that the fraction *f* of the masterbatch polymer that is able to crystallise does so without altering the crystallisation kinetics of the linear material to which the masterbatch is added, we have the following relationship:

$$\Delta H = \frac{10 + 0.6fP}{100 + P} \qquad (3.3)$$

where ΔH is the enthalpy of crystallisation or melting and P is the number of parts masterbatch added to the 90 : 10 BPE : LPE system.

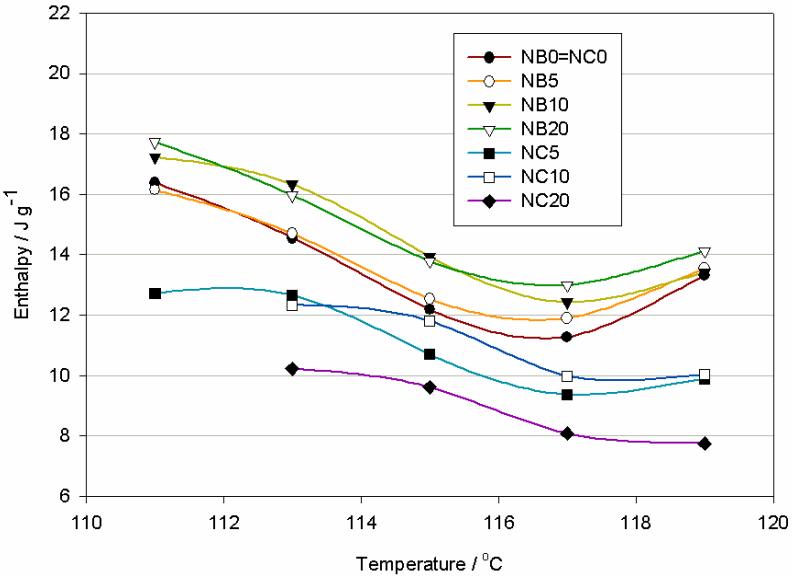

Figure 3.12: Isothermal crystallisation enthalpies for all materials as a function of crystallisation temperature, obtained by integrating the power flow curve as per Figure 3.1. Data are difficult to interpret without estimating the amount of masterbatch host LLDPE involved in the crystallisation process.

By comparing the data corresponding to each of the filled systems to the data for NB0=NC0, where P=0, it is possible to estimate f as a function of temperature and loading level. If f is a function of loading level, it follows that the crystallisation behaviour cannot be considered in terms of a simple arithmetic addition or subtraction of crystallisable material from an unfilled reference system. Estimated values of f are shown in Figure 3.13, where they are described as "predicted equivalent linear material" to emphasise the fact that the comparison is made to the enthalpies liberated by the LPE in NB0=NC0. Although the masterbatches do not contain LPE, chains of LLDPE contain long linear sequences which are able to crystallise into lamellae.

In Figure 3.13, negative values of f are predicted for the Nanocor-based materials, meaning that there must be some other reason for the low crystallinity in these systems than the Nanocor masterbatch not containing any crystallisable polymer. It is sensible to conclude that the clay in these systems serves to reduce the effective mobility of crystallising LPE segments

as they are transported to the crystal growth front. Possible interpretations of this reduced effective mobility are given in section 3.5.

This phenomenon is not as obvious in the Nanoblend-systems, which predict an equivalent linear fraction of ~30 %, though it would explain the fact that NB20 has a smaller *f* than NB10. Figure 3.14 shows the enthalpies of crystallisation and melting for the Nanoblend masterbatch. Compared to

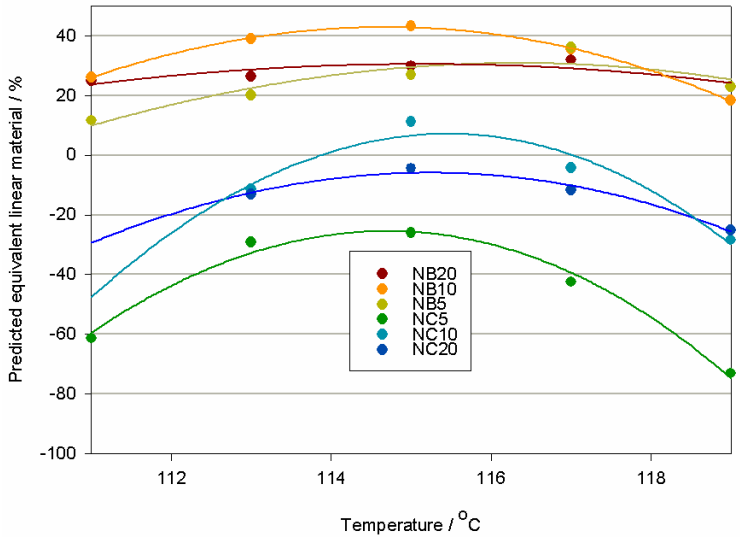

Figure 3.13: Amount of crystallisable material in masterbatches estimated by comparison of data in Figure 3.12 to NB0=NC0 and assuming that the ability of the linear material to crystallise remains unchanged. Cubic fits to aid the eye. Data for Nanoblend-based materials suggests Nanoblend masterbatch is rich in crystallisable material. Negative numbers for Nanocor-based materials show that uncrystallisable masterbatch polymer alone is insufficient to account for reduced crystallinity in blends.

NB0=NC0, these correspond to an equivalent linear fraction, broadly invariant with temperature, of 17%. That this is only around half the value predicted in Figure 3.13 is likely to be due to the effective mobility reduction effect introduced above.

Figures 3.15 and 3.16 repeat this analysis for the enthalpies of melting. Melting enthalpies are larger than crystallisation enthalpies as a result of lamellar thickening processes; they are therefore a function of ramp rate. These data both confirm the conclusions drawn from the crystallisation data

and bring further clarification. It is clear from the melting data that there is a difference between NB20 and NB5 above and beyond any volumetric increase in masterbatch LLDPE. Furthermore, the surprisingly high melt enthalpy shown by NC10 indicates that competing processes are present in both masterbatches both to promote and hinder the crystallisation process.

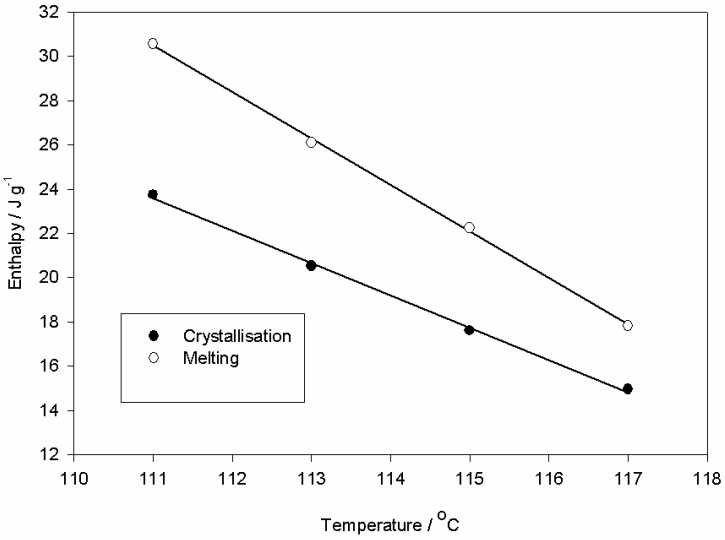

Figure 3.14: Enthalpies of crystallisation and melting for Nanoblend masterbatch.

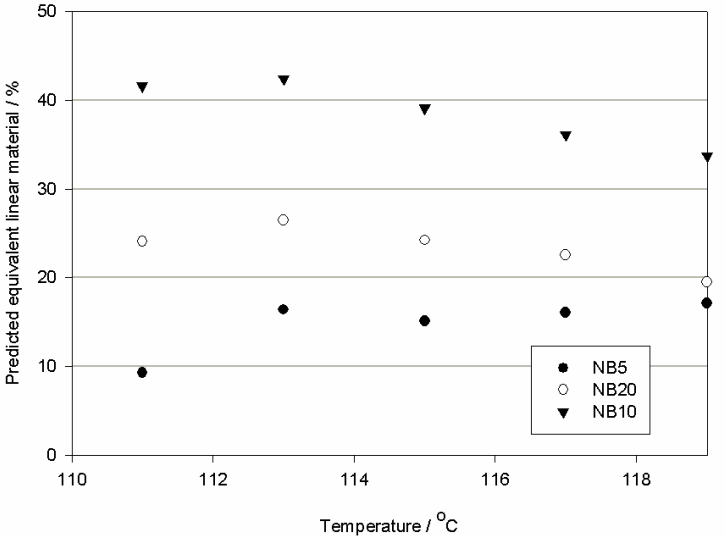

Figure 3.15: As Figure 3.13 but for enthalpies of melting in the Nanoblend-based systems. A clearer distinction between NB5 and NB20 is seen than in the crystallisation enthalpies.

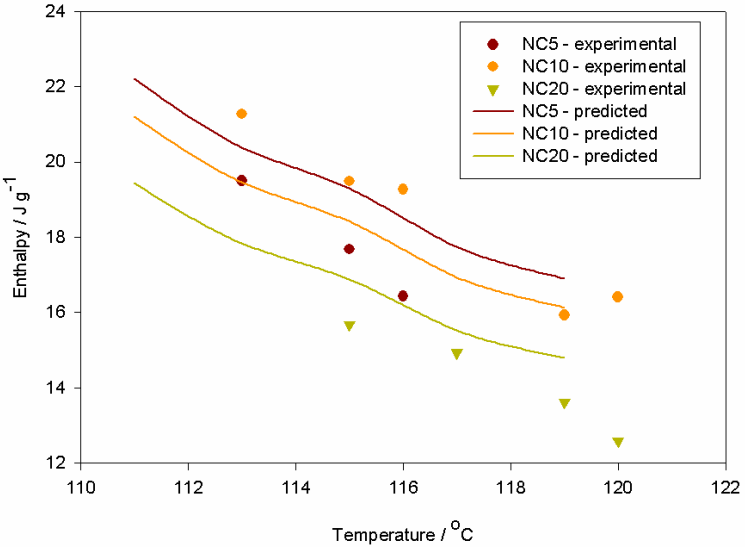

Figure 3.16: Dots: Melting enthalpies for NC5, NC10 and NC20. Lines: Predictions obtained by scaling response of NB0=NC0 using Equation 3.3 with *f* = 0. The melting enthalpy of NC10 is surprisingly high.

3.5 Discussion

In order for the crystallisation of polymer chains onto a nucleus to occur, a free energy balance must be satisfied [3.5]:

$$\Delta G = \sum_i A_i \sigma_i - \Delta g V_{crystal} \qquad (3.4)$$

where ΔG is the overall crystallisation free energy, Δg and σ being the specific volume and surface free energies respectively. $V_{crystal}$ and A_i are the nuclear volume and surface areas. The size of a stable critical nucleus is obtained by setting the differential of 3.4 with respect to *r* to zero. Furthermore, conformational restrictions may come into play below a certain distance. For example, Bhimaraj *et al.*[3.14] observed that whereas polyethylene terephthalate (PET) normally nucleates on Al_2O_3, nucleation was not observed in nano-Al_2O_3 because the particle diameter was below the radius of gyration of the polymer chains.

In the next chapter, SEM images demonstrate that the addition of Nanocor masterbatch leads to a large increase in nucleation density, whereas the Nanoblend masterbatch does not. According to the literature, the effectiveness of MMT as a nucleant is ambiguous [3.15-3.17]. Any nucleation enhancements observed in the literature are small in comparison to the massive internal surface areas provided by the MMT. Montanari [3.18] suggests that any nucleation enhancement seen in MMT systems can be explained by secondary nucleation onto impurities (e.g. alkylammonium chloride) left over from the organocompatibalisation process. This may be in the form of crystals on tactoid surfaces [3.19].

The nucleating activity of MMT can be assessed indirectly by analysis of the depression in equilibrium crystal melting temperature. Xu *et al.* [3.20] considered the case where secondary nucleation occurs between two parallel sheets (an intercalated system.) Three distinct surface energies are defined, as shown in Figure 3.17. In this case, equation 3.4 becomes:

$$\Delta G = 2xl\sigma_1 + 2al\sigma_2 + 2ax\sigma_3 - alx\Delta g \qquad (3.5)$$

where:

$$\Delta g = \Delta h_f - T_m \Delta S_f \approx \Delta h_f - \frac{T_m \Delta h_f}{T_m^0} \qquad (3.6)$$

In equation (3.5), Δh_f and ΔS_f are the enthalpy and entropy of fusion. At the equilibrium melting temperature T_m^0, Δg=0 as the enthalpy-lowering Van der Waals forces between the CH_2 groups exactly balance the entropic drive towards disassociation. Equation 3.5 is not exact as it ignores surface effects and small changes in both Δh_f and ΔS_f with temperature. T_m^0 can be estimated by plotting T_m against T_c and extrapolating to $T_m = T_c$ and then used together with equations 3.4 and 3.5 to estimate σ_1. According to Xu *et al.* [3.20], this leads to a value for the free energy of the PE-MMT interface as low as 1.0 mJ m^{-2}. Being so much smaller than the lateral surfaces (11.8 mJ m^{-2}) or folding surfaces (100 mJ m^{-2}) of PE lamellae, nucleation onto the MMT sheets would be favourable. Precisely how robust this approach is remains to be established.

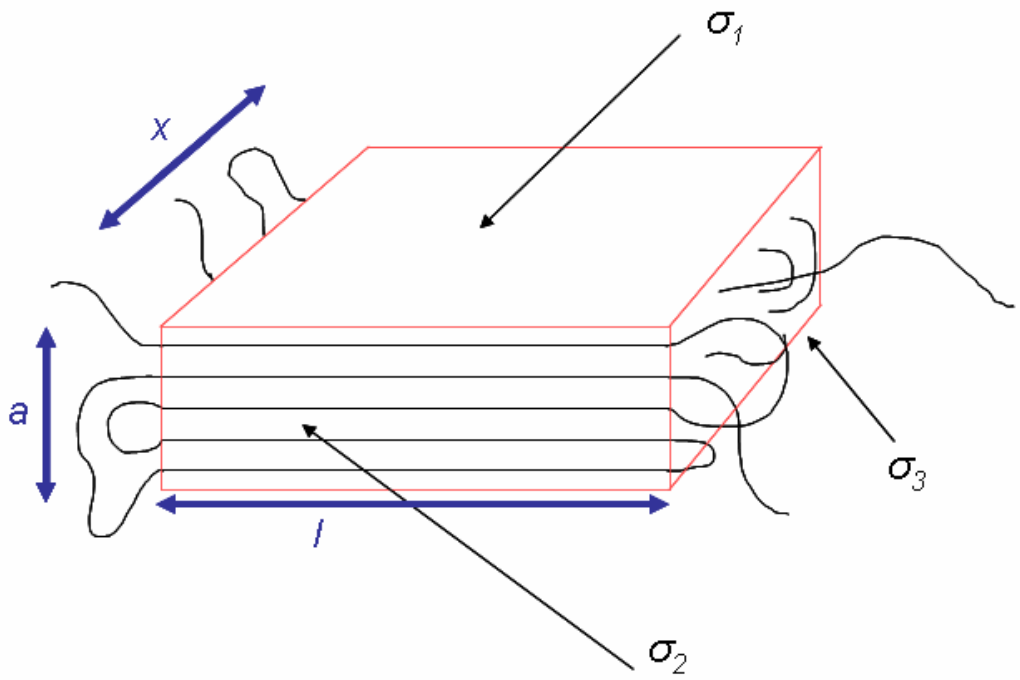

Figure 3.17: Schematic of hypothetical lamella growing between two parallel clay sheets in the *x-l* plane. Adapted from Xu *et al.* [3.20].

The materials studied by Xu *et al.* were well-defined intercalated morphologies produced by in-situ polymerisation, contrary to the systems in this study. Furthermore, initial studies showed that the variation in T_m of <0.4 ℃ found in NB10, NC10 and NB0=NC0 was negligible following crystallisation in a grant WG028 oil bath at 128 ℃ for 60 hours. It was concluded that neither the method of Xu *et al.* nor the more orthodox Hoffmann-Weeks approach, which deals with hypothetical crystals of infinite lateral extent [3.21] are appropriate for these materials.

Xu *at al.* [3.22] have also found massively enhanced growth kinetics in PE-MMT nanocomposites. These researchers also report a change in Avrami dimensionality from ~2.0 to ~3.0 from intercalated to exfoliated systems, suggesting a fundamental change in the geometry of growth. Similar findings are reported by other workers [3.23-3.24]. Di Maio *et al.* [3.25] found that adding MMT to polycaprolactone had this effect, and also noticed that whereas the unfilled samples gave good fits to an Avrami function between 0% and 100% conversion, the filled samples showed substantial deviation above 80%. Linearised Avrami plots for the materials in this work are shown in Figure 3.18. Whereas the unfilled and Nanoblend-based materials do not

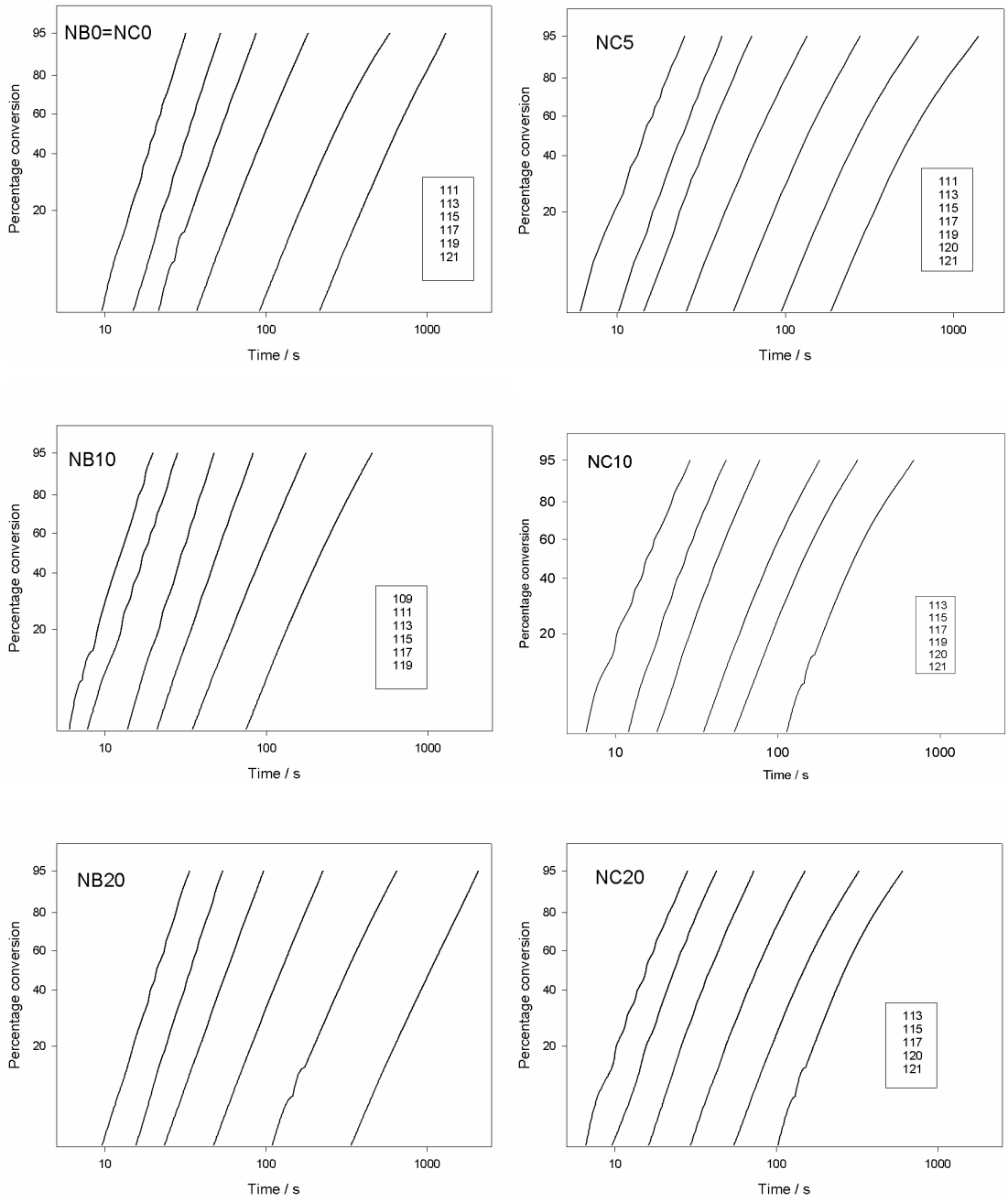

Figure 3.18: Linearised Avrami plots associated with variable shape method. The greater deviation from linearity above 60% conversion occurring in the Nanocor-based materials corresponds to enhanced secondary crystallisation processes.

show any deviation from linearity, significantly slower secondary crystallisation effects are seen at all loading levels of Nanocor, suggesting a considerable reduction in mobility at high degrees of conversion. Note that these effects appear above 60% conversion, and do not therefore affect the K_3 analysis.

Some researchers have made use of Lauritzen-Hoffmann (LH) theory [3.26] in analysing the crystallisation kinetics of nanocomposite systems. This purely enthalpic approach to nucleation predicts three growth regimes corresponding to the relative rates of nucleation and spreading of crystal segments across the growth surface. In Regime I, new layers are only nucleated on completed layers, whereas in Regime III, layers do not have time to complete, leading to highly disordered growth. Regime II, the intermediate case, is operative in LPE below 127 ℃ [3.27].The overall linear growth rate can be expressed as:

$$G = G_0 \exp\left(\frac{-U^*}{R(T-T_\infty)}\right)\exp\left(\frac{-K_g}{T(\Delta T)}\right) \qquad (3.7)$$

where G is the growth rate, U^* is the activation energy for polymer diffusion, R is the gas constant, T is the crystallisation temperature, T_∞ is the thermodynamic glass transition temperature, ΔT is the degree of supercooling and K_g is the nucleation rate constant which is specific to each regime. Tjong and Bao [3.28] have used Regime II LH theory to calculate a reduction of fold surface energy in PE / MMT systems. They used a hotstage to calculate the linear growth rates, calculating the fold surface energy using equation (3.7) together with the Regime II formula for K_g:

$$K_g = \frac{2b\sigma\sigma_e T_m^o}{k\Delta h_f} \qquad (3.8)$$

where σ and σ_e are the lateral and fold surface free energies respectively. The effective chain thickness is given by b.

On the other hand, Regime III kinetics have been observed in PE / MMT nanocomposites prepared by in-situ polymerisation [3.29]. By altering the polymerisation time, the degree of exfoliation was controlled, producing

intercalated and exfoliated samples with 23 %wt and 11 %wt MMT respectively. Since a transition to Regime II kinetics was observed, at 125 ℃, only in the exfoliated sample, it is suggested that the origin of Regime III kinetics was chain immobilisation in the galleries rather than enhanced nucleation.

The work of Xie *et al.* [3.30] is particularly relevant to the current study. Blends of MA-g-PE / MMT were prepared with MMT levels of 1.5%, 3%, 5% and 9% by volume. It was found that in the lowest two concentrations, the clay apparently caused no significant differences in the crystallisation kinetics. The 5% blend, however, displayed faster kinetics. At 9%, however, it was remarked that the conflicting effects of enhanced nucleation and constrained molecular diffusion due to the barrier effect of the clay resulted in more crystal defects and decreased spherulite size.

This reduced segmental mobility scenario is frequently invoked in the literature [3.31-3.32] and seems to be the most likely candidate mechanism for most of the salient results discussed above:

- Non-monotonic dependence of K_3 on loading level for both masterbatches (with a competing enhanced nucleation mechanism.)
- Reduced annealing / increased lamellar thickening in NB10, NB20, NC10 and NC20 during melting, following isothermal crystallisation at low temperatures.
- Non-monotonic prediction of amount of crystallisable polymer in both masterbatches with loading level (with a competing enhanced nucleation mechanism.)

The effective mobility reduction may indeed correspond to a real reduction in chain mobility considered as an intensive property of the matrix. It would be associated with an increase in the glass transition temperature. Alternatively, topological constraints may both increase the effective distance which must be traversed by crystallising segments and reduce the effective cross-sectional area available to these diffusion currents. Liu *et al.* [3.33] found a maximum in the degree of crystallinity in PA / MMT nanocomposites at 5 wt% o-MMT, although they offer an alternative mechanism for the lower crystallinity seen at higher loading levels. For them, as the loading level increases, so

does the probability that a single chain will be attracted to more than one platelet, reducing its net attraction to any one platelet. A third possible mechanism may therefore exist to explain the reduced apparent mobility in systems with enhanced nucleation.

So, to what do we owe the slightly enhanced K_3 and crystallinity behaviour exhibited by NB10? It is possible that the clay is mildly nucleating, but that the MA-g-HDPE does not experience this due to an intrinsically low segmental mobility: based on a fusion enthalpy of 295 J g^{-1} for polyethylene [3.34], the crystallinity of NB0 (MA) varied from 10 % at 114 °C to 27 % at 106 °C with cocrystallisation. In comparison, the crystallinity of NB0 was 35 % at 117 °C and as high as 70 % at 109 °C. Furthermore, the MA-g-LPE crystallises at a lower temperature than the masterbatch polymer. It is possible that by the time the MA-g-LPE starts to crystallise, the clay is covered in already-crystallised LLDPE.

The enhanced kinetics of NB10 could be a result of substantial inhomogeneity in these materials. It is unlikely that NB0=NC0 would experience liquid-liquid phase segregation (LLPS) in this temperature range [3.35]. However, we do not know whether LLPS may be induced between the LPE and BPE via interactions with the masterbatch. Pre-crystallisation interactions in the melt are discussed in more detail in the next chapter. Alternatively, the distribution of masterbatch may itself vary with loading level as a result of having experienced different flow fields in the extruder. The degree of inhomogeneity in the system will determine the distribution of distances which crystallising segments must travel to reach a growth front, thereby affecting their apparent mobilities. This distance distribution is in turn a fraction of the amount of linear material in the system, which is also affected by the masterbatch loading level.

A simple explanation for the enthalpic maxima at 115 °C in Figure 3.10 would be that this is an optimum temperature for cocrystallisation between the LPE and masterbatch LLDPE. The corresponding reduction in the amount of defective material may then explain the suppression of feature “B” at this temperature in Figure 3.11. Further studies over a narrow range of temperatures around 115 °C would be needed to confirm this.

It is unfortunate that this work cannot be compared with the significant amount of the work in the literature which is performed using various forms of

non-isothermal Avrami analysis. This was originally introduced by Ozawa [3.36], who invoked the use of a so-called "cooling function" X_c:

$$C(T) = 1 - \exp\left[\frac{-\chi_c(T)}{A^{m+2}}\right] \qquad (3.9)$$

$$\chi_c = \int_{T_m}^{T} N_c(\vartheta)\left[\int_{T_m}^{T} v(T)\cdot dT - \int_{T_m}^{\vartheta} v(T)\cdot dT\right]^m \nu(\vartheta)\cdot d\vartheta \qquad (3.10)$$

where C(T) is the fractional conversion as a function of temperature, A and m being the growth and dimensionality factors. T, T_m and θ are the current temperature, the temperature above which crystallisation does not occur and the temperature defining the cut-off point for objects able to reach a point P. N_c is the nucleation density, v(T) the linear growth rate and *v* the nucleation rate. The only way to render equation 3.9 at all tractable is to impose strict assumptions on the crystal growth. Nucleation and growth must obey strict Arrhenius-type temperature dependence. However, in their classic work [3.37], Fisher and Turnbull derive Arrhenius behaviour for nucleation only under equilibrium conditions. On top of this, estimates of crystallisation free energy obtained from non-isothermal Avrami have been demonstrated to be invalid [3.38].

3.6 Conclusions

The isothermal crystallisation behaviour of these materials is remarkably different depending on which masterbatch is used. Whereas the Nanocor-based materials have a massively increased effective 3D crystallisation rate parameter, this is not the case in the Nanoblend-based materials. It appears that in both sets of materials, competition exists between distinct mechanisms for enhanced and reduced crystallisation kinetics. As a result of this, both masterbatches demonstrate maxima in both K_3 and crystallisation enthalpy as a function of loading level. At sufficiently low crystallisation temperatures, the isothermal lamellae of highly-filled systems are more disordered than the other systems, as demonstrated by enhanced lamellar thickening and reduced annealing upon melting.